

# Detection of slow slip events using wavelet analysis of GNSS recordings

Ariane Ducellier<sup>1</sup>, Kenneth C. Creager<sup>1</sup>, and David A. Schmidt<sup>1</sup>

<sup>1</sup>University of Washington, Department of Earth and Space Sciences, Box 351310, 4000 15th Avenue NE Seattle, WA 98195-1310

## Key points

- 8 • We use a wavelet-based signal processing method to detect transients in  
9 GNSS data, such as slow slip events.

10 • There is a good correlation between detections using GNSS data and in-  
11 dependent detections using seismic data.

12 • The method could be applied in regions where no tremor are detected in  
13 conjunction with slow slip events.

14    **Abstract**

15    In many places, tectonic tremor is observed in relation to slow slip and can  
16    be used as a proxy to study slow slip events of moderate magnitude where  
17    surface deformation is hidden in Global Navigation Satellite System (GNSS)  
18    noise. However, in subduction zones where no clear relationship between tremor  
19    and slow slip occurrence is observed, these methods cannot be applied, and we  
20    need other methods to be able to better detect and quantify slow slip. Wavelets  
21    methods such as the Discrete Wavelet Transform (DWT) and the Maximal  
22    Overlap Discrete Wavelet Transform (MODWT) are mathematical tools for  
23    analyzing time series simultaneously in the time and the frequency domain by  
24    observing how weighted differences of a time series vary from one period to the  
25    next. In this paper, we use wavelet methods to analyze GNSS time series and  
26    seismic recordings of slow slip events in Cascadia. We use detrended GNSS  
27    data, apply the MODWT transform and stack the wavelet details over several  
28    nearby GNSS stations. As an independent check on the timing of slow slip  
29    events, we also compute the cumulative number of tremor in the vicinity of the  
30    GNSS stations, detrend this signal, and apply the MODWT transform. In both  
31    time series, we can then see simultaneous waveforms whose timing corresponds  
32    to the timing of slow slip events. We assume that there is a slow slip event  
33    whenever there is a positive peak followed by a negative peak in the wavelet  
34    signal. We verify that there is a good correlation between slow slip events  
35    detected with only GNSS data, and slow slip events detected with only seismic  
36    data for northern Cascadia. The wavelet-based detection method detects well  
37    events of magnitude higher than 6 as determined by independent event catalogs  
38    (e.g. [Michel et al., 2019]).

39    **1 Introduction**

40    Slow slip events are a new feature discovered in the last two decades in many  
41    subduction zones thanks to recordings of the displacement of Earth's surface by  
42    dense Global Navigation Satellite System (GNSS) networks. As with ordinary  
43    earthquakes, slow slip events represent slip on a fault, for instance the plate  
44    boundary between a tectonic plate subducting under another tectonic plate.  
45    However, they take a much longer time (several days to several years) to happen  
46    relative to ordinary earthquakes. They have a relatively short recurrence  
47    time (months to years) compared to the recurrence time of regular earthquakes  
48    (up to several hundreds of years), allowing scientists to observe and study many  
49    complete event cycles, which is typically not possible to explore with traditional  
50    earthquake catalogs [Beroza and Ide, 2011]. A slow slip event on the plate  
51    boundary is inferred to happen when there is a reversal of the direction of motion  
52    at GNSS stations, compared to the secular interseismic motion. Slow slip  
53    events have been observed in many places, such as Cascadia, Nankai (southwest  
54    Japan), Alaska, Costa Rica, Mexico, and New Zealand [Beroza and Ide, 2011,  
55    Audet and Kim, 2016].

56  
57 In many places, tectonic tremor is also observed in relation to slow slip, but  
58 it is more abundant in some places. Tremor is a long (several seconds to many  
59 minutes), low amplitude seismic signal, with emergent onsets, and an absence  
60 of clear impulsive phases. Tectonic tremor have been explained as a swarm of  
61 small, low-frequency earthquakes (LFEs) [Shelly et al., 2007], which are small  
62 magnitude earthquakes ( $M \sim 1$ ) for which frequency content (1-10 Hz) is lower  
63 than for ordinary earthquakes (up to 20 Hz). In subduction zones such as Nankai  
64 and Cascadia, tectonic tremor observations are spatially and temporally corre-  
65 lated with slow slip observations [Obara, 2002, Rogers and Dragert, 2003]. Due  
66 to this correlation, these paired phenomena have been called Episodic Tremor  
67 and Slip (ETS). However, this is not always the case. For instance, in northern  
68 New Zealand, tremor are more challenging to detect, and seem to be located  
69 downdip of the slow slip on the plate boundary [Todd and Schwartz, 2016]. In  
70 Alaska, the tremor zone only partially overlaps the long-term slow slip zone and  
71 there does not appear to be any temporal correlation between tremor and slow  
72 slip occurrence [Wech, 2016].

73  
74 In Cascadia and Guerrero, Mexico, tremor has been used as a proxy to ob-  
75 serve slow slip events that are not directly observed in the GNSS data. For  
76 instance, Aguiar et al. [2009] studied 23 ETS events in Cascadia with more  
77 than 50 hours of tectonic tremor. For all these events, they computed both  
78 the GPS-estimated moment release and the cumulative number of hours of tec-  
79 tonic tremor recorded. They observed a linear relationship between moment  
80 release and number of hours of tremor for ETS events of moment magnitude  
81 6.3 to 6.8. They also observed many smaller bursts of tremor of duration 1 to  
82 50 hours in between the big ETS events, without any detectable signal in the  
83 GPS data. However, based on the relationship between slow slip moment and  
84 number of hours of tremor for bigger events, it is possible to infer the existence  
85 of smaller slow slip events of magnitude 5-6 occurring simultaneously with the  
86 tremor bursts.

87  
88 Frank [2016] divided GPS time series observations from Guerrero and Cas-  
89 cadia into two groups: the first group contains days with abundant tremor and  
90 LFEs, the second group contains days when the number of tremor or LFEs is  
91 lower than a threshold. He then stacked separately the two groups of daily  
92 observations and observed a cumulative displacement in the northern direction  
93 (for Guerrero) and the eastern direction (for Cascadia) corresponding to the  
94 loading period when few tremor or LFEs are observed and the surface defor-  
95 mation corresponds to the secular plate motion. He also observed a cumulative  
96 displacement in the southern direction (for Guerrero) and the western direction  
97 (for Cascadia) corresponding to the release period when tremor and LFEs are  
98 observed. He was thus able to observe a reverse displacement corresponding to  
99 smaller slow slip events not directly observable in the GPS data for individual  
100 events.

101

102 However, in other subduction zones such as New Zealand, there is no clear  
103 relationship between tremor and slow slip occurrence and these methods cannot  
104 be applied to detect smaller slow slip events that produce a GNSS signal with  
105 an amplitude too small compared to the noise. We thus need other methods to  
106 be able to better detect and quantify slow slip.

107

108 Wavelets methods such as the Discrete Wavelet Transform (DWT) are math-  
109 ematical tools for analyzing time series simultaneously in the time and the fre-  
110 quency domain by observing how weighted differences of a time series vary from  
111 one period to the next. Wavelet methods have been widely used for geophysical  
112 applications (e.g. [Kumar and Foufoula-Georgiou, 1997]). However, few studies  
113 have used wavelet methods to analyze recordings of slow slip, and their scope  
114 was limited to the detection of the bigger (magnitude 6-7) short-term (a few  
115 weeks) events [Szeliga et al., 2008, Ohtani et al., 2010, Wei et al., 2012, Alba  
116 et al., 2019].

117

118 Szeliga et al. [2008] determined the timing and the amplitude of 34 slow  
119 slip events throughout the Cascadia subduction zone between 1997 and 2005  
120 using wavelets. They modeled the GPS time series by the sum of a linear trend,  
121 annual and biannual sinusoids representing seasonal effects, Heaviside step func-  
122 tions corresponding to earthquakes and hardware upgrades, and a residual sig-  
123 nal. They then applied a Gaussian wavelet transform to the residual time series  
124 to get the exact timing of slow slip at each GPS station. The idea is that the  
125 wavelet transform allows us to analyze the signal both in the time and the fre-  
126 quency domains. A sharp change in the signal will be localized and seen at all  
127 levels of the wavelet decomposition, contrary to what happens with the periodic  
128 sinusoids of the Fourier transform.

129

130 Instead of using wavelets in the time domain, Ohtani et al. [2010] used 2D  
131 wavelet functions in the spatial domain to detect slow slip events. They de-  
132 signed the Network Stain Filter (NSF) to detect transient deformation signals  
133 from large-scale geodetic arrays. They modeled the position of the GPS station  
134 by the sum of the secular velocity, a spatially coherent field, site-specific noise,  
135 reference frame errors, and observation errors. The spatial displacement field is  
136 modeled by the sum of basis wavelets with time-varying weights. Their method  
137 has been successfully used to detect a transient event in the Boso peninsula,  
138 Japan, and a slow slip event in the Alaska subduction zone [Wei et al., 2012].

139

140 Finally, Alba et al. [2019] used hourly water level records from four tide  
141 gauges in the Juan de Fuca Straight and the Puget Sound to determine vertical  
142 displacements, uplift rates between ETS events, and net uplift rates between  
143 1996 and 2011. Their main idea is that the tidal level measured at a given  
144 gauge is the sum of a noise component at multiple timescales (tides, ocean  
145 and atmospheric noise) and an uplift signal due to the ETS events. The noise  
146 component is assumed to be coherent between all tidal gauges, while the uplift  
147 signal is different provided that the gauges are far enough from each other. By

stacking the tidal records, the uplift signals cancel each other while the noise signal is amplified. By stacking the details of the DWT decomposition, instead of stacking the raw tidal record, each of the components of the noise at different time scales is retrieved and can then be removed from the raw records to obtain the uplift signal. The authors were then able to clearly see a difference in uplift between the two tidal gauges at Port Angeles and Port Townsend.

In our study, we use a similar approach with a different reasoning. We only stack signals at nearby GPS stations, assuming that the longitudinal displacement due to the ETS events will then be the same at each of the GPS stations considered. We suppose that some of the noise component is different at each GPS station and will be eliminated by the stacking. Finally, we suppose that the noise and the longitudinal displacement due to the ETS events and the secular plate motion have different time scales, so that the wavelet decomposition will act as a bandpass filter to retrieve the displacement signal and highlight the ETS events. We use wavelet methods to analyze GPS and seismic recordings of slow slip events in Cascadia. Our objective is to verify that there is a good correlation between slow slip events detected with only GNSS data, and slow slip events detected with only seismic data. We thus want to demonstrate that the wavelet-based detection method can be applied to detect slow slip events that may be currently undetected with standard methods.

## 2 Data

We focused our study on northwest Washington State. For the GNSS data, we used the GPS time series provided by the Pacific Northwest Geodetic Array, Central Washington University. These are network solutions in ITRF2008 with phase ambiguities resolved. Solutions are computed with JPL/NASA orbits and satellite clocks. North, East, and Vertical directions are available. However, as the direction of the secular plate motion is close to the East direction, we only used the East direction of the GPS time series for the data analysis, as it has the best signal-to-noise ratio. The wavelet method works best with data with zero mean, and no sharp discontinuities, so we use the cleaned dataset, that is GPS times series with linear trends, steps due to earthquakes or hardware upgrades, and annual and semi-annual sinusoids signals simultaneously estimated and removed following Szeliga et al. [2004]. For the seismic data, we used the tremor catalog from reference for the catalog. The following is to be modified. the Pacific Northwest Seismic Network (PNSN) [Wech, 2010]. Tremor were detected and located using waveform envelope correlation and clustering and a centroid location is available for every given five-minute time window when tremor was detected. As the catalog starts in August 2009, we only looked at GPS data recorded in 2009 or later.

190 **3 Method**

191 **3.1 The Maximal Overlap Discrete Wavelet Transform**

192 The Discrete Wavelet Transform (DWT) is an orthonormal transform that  
 193 transforms a time series  $X_t$  ( $t = 0, \dots, N - 1$ ) into a vector of wavelet coeffi-  
 194 cients  $W_i$  ( $i = 0, \dots, N - 1$ ). If we denote  $J$  the level of the wavelet decom-  
 195 position, and we have  $N = n * 2^J$ , where  $n$  is some integer higher or equal to 1,  
 196 the vector of wavelet coefficients can be decomposed into  $J$  wavelet vectors  $W_j$   
 197 of lengths  $\frac{N}{2}, \frac{N}{4}, \dots, \frac{N}{2^J}$ , and one scaling vector  $V_J$  of length  $\frac{N}{2^J}$ . Each wavelet  
 198 vector  $W_j$  is associated with changes on scale  $\tau_j = dt2^{j-1}$ , where  $dt$  is the time  
 199 step of the time series, and corresponds to the filtering of the original time series  
 200 with a filter with nominal frequency interval  $[\frac{1}{dt2^{j+1}}; \frac{1}{dt2^j}]$ . The scaling vector  
 201  $V_J$  is associated with averages in scale  $\lambda_J = dt2^J$ , and corresponds to the fil-  
 202 tering of the original time series with a filter with nominal frequency interval  
 203  $[0; \frac{1}{dt2^{j+1}}]$ . We can also define for  $j = 1, \dots, J$  the  $j$ th wavelet detail  $D_j$ , which  
 204 is a vector of length  $N$ , and is associated to scale  $\tau_j = dt2^{j-1}$ . Similarly, we can  
 205 define for  $j = 1, \dots, J$  the  $j$ th wavelet smooth  $S_j$ , which is a vector of length  
 206  $N$ , and is associated to scales  $\tau_{j+1} = dt2^{j+1}$  and higher. Together, the details  
 207 and the smooths define the multiresolution analysis (MRA) of  $X$ :

208

$$X = \sum_{j=1}^J D_j + S_J \quad (1)$$

209 The DWT present several disadvantages. First, the length of the time se-  
 210 ries must be a multiple of  $2^J$  where  $J$  is the level of the DWT decompositon.  
 211 Second, the time step of the wavelet vector  $W_j$  is  $dt2^j$ , which may not corre-  
 212 spond to the time when some interesting phenomenon is visible on the original  
 213 time series. Third, when we circularly shift the time series, the corresponding  
 214 wavelet coefficients, details and smooths are not a circularly shifted version of  
 215 the wavelet coefficients, details and smooths of the original time series. Thus,  
 216 the values of the wavelet coefficients, details and smooths are strongly depen-  
 217 dent on the time when we start experimentally gathering the data. Finally,  
 218 when we filter the time series to obtain the details and smooths, we introduce  
 219 a phase shift, which makes difficult to line up meaningfully the features of the  
 220 MRA with the original time series.

221

222 This is why we use instead the Maximal Overlap Discrete Wavelet Transform  
 223 (MODWT). The MODWT transforms the time series  $X_t$  ( $t = 0, \dots, N - 1$ ) into  $J$   
 224 wavelet vectors  $\tilde{W}_j$  ( $j = 1, \dots, J$ ) of length  $N$  and a scaling vector  $\tilde{V}_J$  of length  
 225  $N$ . As is the case for the DWT, each wavelet vector  $\tilde{W}_j$  is associated with  
 226 changes on scale  $\tau_j = dt2^{j-1}$ , and corresponds to the filtering of the original time  
 227 series with a filter with nominal frequency interval  $[\frac{1}{dt2^{j+1}}; \frac{1}{dt2^j}]$ . The scaling  
 228 vector  $\tilde{V}_J$  is associated with averages in scale  $\lambda_J = dt2^J$ , and corresponds to the  
 229 filtering of the original time series with a filter with nominal frequency interval  
 230  $[0; \frac{1}{dt2^{j+1}}]$ . As is the case for the DWT, we can write the MRA:

$$X = \sum_{j=1}^J \tilde{D}_j + \tilde{S}_J \quad (2)$$

The MODWT of a time series can be defined for any length  $N$ . The time step of the wavelet vectors  $\tilde{W}_j$  and the scaling vector  $\tilde{V}_J$  is equal to the time step of the original time series. When we circularly shift the time series, the corresponding wavelet vectors, scaling vector, details and smooths are shifted by the same amount. The details and smooths are associated with a zero phase filter, making it easy to line up meaningfully the features of the MRA with the original time series. The wavelet methods for time series analysis are explained in a more detailed way in [Percival and Walden, 2000]).

240

### 3.2 Application to synthetic data

To illustrate the wavelet transform method, we first apply the MODWT to synthetics data. As slow slip events occur in Cascadia on a regular basis, every twelve to eighteen months, we create a synthetic signal of period  $T = 500$  days. To reproduce the ground displacement observed on the longitudinal component of GPS stations in Cascadia, we divide each period into two parts: In the first part of duration  $T - N$ , the displacement is linearly increasing and corresponds to the secular plate motion in the eastern direction; in the second part of duration  $N$ , the displacement is linearly decreasing and corresponds to a slow slip event on a reverse fault at depth triggering a ground displacement in the western direction. To see the effect of the magnitude of the slow slip event, we use different values for  $N = 5, 10, 20, 40$  days. Figure 1 shows the synthetics, the details of the wavelet decomposition for levels 1 to 10, and the smooth for the four durations of a slow slip event.

255

The ramp-like signal is transformed through the wavelet filtering into a waveform with first a positive peak and then a negative peak. The shape of the waveform is the same for every level of the wavelet decomposition, but the width of the waveform increases with the scale level. For the 8th level of the wavelet decomposition, the width of the waveform is nearly as large as the time between two events. At larger scales, the waveforms start to merge two contiguous events together, and make the wavelet decomposition less interpretable. For an event of duration 5 days, the wavelet details at levels higher than 3 have a larger amplitude than the wavelet details at lower scales. For an event of duration 10 days, the wavelet details at levels higher than 4 have a larger amplitude than the wavelet details at lower scales. For an event of duration 20 days, the wavelet details at levels higher than 5 have a larger amplitude than the wavelet details at lower scales. For an event of duration 40 days, the wavelet details at levels higher than 6 have a larger amplitude than the wavelet details at lower scales. Thus, the scale levels at which an event is being seen in the wavelet details give us an indication about the duration (and the magnitude) of the slow slip event.

272 We expect the big slow slip events of magnitude 6-7 that last several weeks to  
273 start being visible at the level 5 of the wavelet decomposition, but to not be  
274 noticeable at lower time scales.

275

### 276 3.3 MODWT of GPS and tremor data

277 The DWT and MODWT methods must be used on a continuous time series,  
278 without gaps in the recordings. To deal with the gaps in the GNSS record-  
279 ings, we simply replace the missing values by the sum of a straight line and a  
280 Gaussian noise component with mean zero and standard deviation equal to the  
281 standard deviation of the whole time series. The straight line starts at the mean  
282 of the five days before the gap and ends at the mean of the five days after the  
283 gap. We verify how the wavelet details may be affected by looking at a GPS  
284 time series without missing values and comparing the wavelet details with and  
285 without removing some data points. Station PGC5 has recorded during 1390  
286 days between 2009 and 2013, without any missing values. We first computed  
287 the wavelet details without missing values. Then, we removed ten neighboring  
288 missing values, replaced them by the sum of the straight line and the Gaussian  
289 noise component, and computed the wavelet details with the replaced values.  
290 Figure 2 shows a comparison of the two wavelet details for two different loca-  
291 tions of the missing values. We can see that there are visible differences in the  
292 time series itself, and in the details at the smallest levels of the wavelet decom-  
293 position. However, the differences between the wavelet details with and without  
294 missing values get smaller and smaller with increasing levels the details, and are  
295 barely visible for the levels we are mostly interested in (levels 6 and above). We  
296 thus conclude that we can easily replace the missing values in the GNSS time  
297 series without introducing false detections of slow slip events.

298

299 We then applied the wavelet filtering to real GPS data. Figure 3 shows the  
300 longitudinal displacement for GPS station PGC5, located in southern Vancou-  
301 ver Island, the details of the wavelet decomposition for levels 1 to 8, and the  
302 smooth. In the data, we can see a sharp drop in displacement whenever there  
303 is a slow slip event. For levels 5 to 8, we can see in the details a positive peak  
304 followed by a negative peak whenever there is a drop in displacement in the  
305 data. We thus verify that the wavelet method can detect slow slip events.

306

307 To increase the signal-to-noise ratio and be able to better detect slow slip  
308 events, we stack the signal over several GPS stations. We choose to focus on  
309 GPS stations located close enough to the tremor zone to get a sufficiently high  
310 amplitude of the slow slip signal. We choose 16 points located on the 40 km  
311 depth contour of the plate boundary (model from Preston et al. [2003]) with  
312 spacing equal 0.1 degree in latitude (red triangles on Figure 4). Then we took  
313 all the GPS stations located in a 50 km radius for a given point, compute the  
314 wavelet details for the longitudinal displacement of each station, and stack each  
315 detail over the GPS stations. We thus have a stacked detail for each level 1 to

316 10 of the wavelet decomposition.

317

318 To compare slow slip events detected with GPS data and slow slip events  
319 detected with seismic data, we took all the tremor epicenters located within  
320 a 50 km radius centered on one of the 16 locations marked by red triangles  
321 on Figure 3. Then we computed the cumulative number of tremor within this  
322 circle. Finally, we removed a linear trend from the cumulative tremor count,  
323 and applied the wavelet transform. Figure 5 shows an example of the wavelet  
324 decomposition for the third northernmost location on Figure 4 (which is closest  
325 to GPS station PGC5). Contrary to what happens for the GPS data, we see a  
326 sharp increase in the data whenever there is a tremor episode, which translates  
327 into a negative peak followed by a positive peak in the wavelet details.

## 328 4 Results

329 We stacked the 8th level detail of the wavelet decomposition of the displacement  
330 over all the GPS stations located in a 50 km radius of a given point, for  
331 the 16 locations indicated in Figure 3. The result is shown in the top panel of  
332 Figure 6, where each line represents one of the locations. To better highlight  
333 the peaks in the wavelet details, we highlighted in red the time intervals where  
334 the amplitude of the stacked detail is higher than a threshold, and in blue the  
335 time intervals where the amplitude of the stacked detail is lower than minus  
336 the threshold. To compare the GPS signal with the tremor signal, we plotted  
337 the 8th level detail of the wavelet decomposition of the tremor count on the  
338 bottom panel of Figure 6. We used the opposite of the cumulative tremor count  
339 for the wavelet decomposition in order to be able to match positive peaks with  
340 positive peaks and negative peaks with negative peaks. In the tremor catalog  
341 from [reference?](#), there are 17 tremor events with more than 150 hours of tremor  
342 recorded. The events are summarized in Table 1. The time of the event is the  
343 start date plus half the duration of the event. Although the latitudinal extension  
344 of the events is not always the same for the GPS data and for the tremor data,  
345 we identify the same 13 events in both 8th wavelet decompositions for the 8th  
346 level: January 2007, May 2008, May 2009, August 2010, August 2011, September  
347 2012, September 2013, August-November 2014, January 2016, March 2017,  
348 June 2018, March-November 2019, and October 2020-January 2021. Although  
349 there are two events in the tremor catalog in August 2014 and November 2014,  
350 these two events are not distinguishable in the 8th level details and look more  
351 like a single event slowly propagating from South to North. The same phe-  
352 nomenon is observed in 2019 when two tremor events in March and November  
353 2019 are merged into a single event propagating slowly from South to North.  
354 In 2020-2021, the wavelet decomposition of the tremor shows one event in the  
355 south in October-November 2020 and one event in the North in January 2021,  
356 but in the wavelet decomposition of the GPS data, these three events look like  
357 a single event propagating slowly from South to North.

358

359 Figures 7 and 8 show the same comparison between the wavelet decomposi-  
360 tion of the GPS data and the wavelet decomposition of the tremor count data  
361 for the 7th level and the 6th level respectively. The events are harder to see in  
362 the 7th level than in the 8th level, both for the GPS data and the tremor count  
363 data. The wavelet decomposition is more noisy for the GPS data between 2010  
364 and 2012, but it does not seem that there are more slow slip events visible in  
365 the 7th level.

366

367 For the 6th level detail, we see an additional event in the South in Fall 2009  
368 that is present both in the GPS and the tremor data. It may correspond to the  
369 northern extent of a big ETS event occurring in Fall 2009 south of the study  
370 area (event 19 in the Michel et al. [2019] catalog). There are three small signals  
371 in the GPS data in Spring 2012, Fall 2017, and Winter 2020 that are not present  
372 in the tremor data, and are probably false detections. To summarize, all the  
373 13 events present on the 8th level detail of the wavelet decomposition are true  
374 detections, 14 of the 17 events present on the 6th level detail of the wavelet  
375 decomposition are true detections.

376

## 377 5 Discussion

378 To better evaluate the number of true and false detections, we convert the  
379 wavelet details into binary time series. If the absolute value of the wavelet  
380 detail is higher than a threshold, we replace the value by 1 (for positive values)  
381 or -1 (for negative values), otherwise we replace the value by 0. We do this  
382 on both the wavelet details of the GPS data and of the tremor data. Then we  
383 decide that if both the GPS and the tremor time series take the value 1 (or  
384 both take the value -1), we have a true detection (true positive TP). If the GPS  
385 and the tremor time series have opposite signs, or if the absolute value of the  
386 GPS time series is 1 but the value of the tremor time series is 0, we have a  
387 false detection (false positive FP). If both time series take the value 0, we do  
388 not have detection (true negative TN). If the GPS time series take the value 0,  
389 but the absolute value of the tremor time series is 1, we miss a detection (false  
390 negative). We then define the sensitivity (true positive rate) and the specificity  
391 (equal to 1 minus the false positive rate) as:

$$\text{sensitivity} = \frac{TP}{TP + FN}$$
$$\text{specificity} = \frac{TN}{TN + FP} \quad (3)$$

392 We can then evaluate the quality of the detections obtained with our method  
393 by plotting a receiver operating characteristic curve (ROC curve). The ROC  
394 curve is widely used for binary classification problems, and is plotted by varying  
395 the values of the threshold (here the thresholds used to convert the GPS and  
396 the tremor time series into binary time series), computing the corresponding

397 values of the true positive rate and the false positive rate (equal to 1 minus the  
398 specificity), and plotting the true positive rate as a function of the false positive  
399 rate. If the classification was made randomly, all the points would fall on the  
400 first diagonal. If the classifier was perfect, the corresponding point would fall  
401 on the top left corner of the graph with true positive rate equal to 1 and false  
402 positive rate equal to 0. The bigger the area under the curve, the better the  
403 classifier is.

404

405 As the slow slip events are better seen on levels 6, 7 and 8 of the wavelet  
406 decomposition, we first add the wavelet details corresponding to levels 6 to 8,  
407 and transform the resulting time series into a binary time series. We apply  
408 this transform to both the GPS and the tremor time series with varying thresh-  
409 olds. We then plot the ROC curve on Figure 9. The corresponding sums of  
410 the wavelet details for the GPS data and the tremor data are shown on Figure  
411 10. We can see that there is a trade-off between sensitivity and specificity. If  
412 we decrease the false positive rate, we also decrease the number of true events  
413 detected. If we increase the number of true events detected, we also increase the  
414 false positive rate. In Figure 10, we have chosen thresholds for the GPS time  
415 series and the tremor time series such that the specificity is higher than 0.75,  
416 and the sensitivity is the highest possible.

417

418 In addition to the magnitude 6 events discussed above, Michel et al. [2019]  
419 have also identified several magnitude 5 events using a variational Bayesian In-  
420 dependent Component Analysis (vbICA) decomposition of the signal. As we  
421 expect smaller magnitude events to be more visible at smaller time scales of  
422 the wavelet decomposition (level 5), we verify for all these events whether a  
423 signal can be seen at the same time as the time given in their catalog. Most  
424 of these magnitude 5 events are also sub-events of bigger magnitude 6 events.  
425 Table 2 summarizes for each event its timing, its number and its magnitude as  
426 indicated in the catalog from Michel et al. [2019], and whether it is part of a  
427 bigger magnitude 6 event.

428

429 Figure 11 shows the 5th level detail wavelet decomposition of the GPS data.  
430 Red lines show the timing of the big ETS events from Table 1, and blue lines  
431 show the timing of the small slow slip events from Table 2.

432

433 All 14 events that are sub-event of a bigger event are visible at level 5.  
434 However, this may be due because the bigger event are clearly seen at levels 6  
435 to 8, and also at smaller time scales. The one small event that is not part of  
436 a bigger event (Winter 2009) is visible at level 5 of the wavelet decomposition.  
437 However, some other events that are not in Michel et al. [2019]'s catalog are  
438 also visible in late 2007, early 2010, early 2012, and late 2016. Therefore, it is  
439 difficult to make the difference between a true detection and a false detection,  
440 and to conclude whether the method can indeed detect events of magnitude 5.

440 **6 Conclusion**

441 In this paper, we have used wavelet methods to analyze GNSS time series and  
442 seismic recordings of slow slip events in Cascadia. We used detrended GNSS  
443 data, applied the MODWT transform and stack the wavelet details over several  
444 nearby GNSS stations. As an independent check on the timing of slow slip  
445 events, we also computed the cumulative number of tremor in the vicinity of  
446 the GNSS stations, detrended this signal, and applied the MODWT transform.  
447 In both time series, we could then see simultaneous waveforms whose timing  
448 corresponds to the timing of slow slip events. We assumed that there is a slow  
449 slip event whenever there is a peak in the wavelet signal. We verified that  
450 there is a good correlation between slow slip events detected with only GNSS  
451 data, and slow slip events detected with only seismic data. The wavelet-based  
452 detection method detects all events of magnitude higher than 6 as determined  
453 by independent event catalogs (e.g. [Michel et al., 2019]). We detected signals  
454 in the GPS data that could be magnitude 5 events, but it is not easy to make  
455 the difference between true detections and false detections.

456 **Data and Resources**

457 The GPS recordings used for this analysis can be downloaded from the PANGA  
458 website [GPS/GNSS Network and Geodesy Laboratory: Central Washington  
459 University, other/seismic network, 1996] <http://www.panga.cwu.edu/>. Reference  
460 for tremor catalog. The Python scripts used to analyze the data and  
461 make the figures can be found on the first author's Github account <https://github.com/ArianeDucellier/slowslip>. Figure 4 was done using GMT  
462 [Wessel and Smith, 1991].

464 **Acknowledgements**

465 This work was funded by the grant from the National Science Foundation XXX.  
466 A.D. would like to thank Pr Donald Percival for introducing her to wavelet  
467 methods during his excellent class taught at University of Washington.

468 **Declaration of Competing Interests**

469 The authors declare no competing interests.

470 **References**

- 471 A.C. Aguiar, T.I. Melbourne, and C.W. Scrivner. Moment release rate of Cas-  
472 cadia tremor constrained by GPS. *Journal of Geophysical Research*, 114:  
473 B00A05, 2009.

- 474 S. Alba, R. J. Weldon, D. Livelybrooks, and D. A. Schmidt. Cascadia ETS  
475 events seen in tidal records (1980–2011). *Bulletin of the Seismological Society*  
476 *of America*, 2019.
- 477 P. Audet and Y.H. Kim. Teleseismic constraints on the geological environment  
478 of deep episodic slow earthquakes in subduction zone forearcs: A review.  
479 *Tectonophysics*, 670:1–15, 2016.
- 480 G.C. Beroza and S. Ide. Slow earthquakes and nonvolcanic tremor. *Annual*  
481 *Review of Earth and Planetary Sciences*, 39:271–296, 2011.
- 482 W.B. Frank. Slow slip hidden in the noise: The intermittence of tectonic release.  
483 *Geophysical Research Letters*, 43:10125–10133, 2016.
- 484 GPS/GNSS Network and Geodesy Laboratory: Central Washington University,  
485 other/seismic network. Pacific Northwest Geodetic Array (PANGA), 1996.  
486 URL <http://www.panga.cwu.edu/>.
- 487 P. Kumar and E. Foufoula-Georgiou. Wavelet analysis for geophysical applica-  
488 tions. *Reviews of Geophysics*, 35(4):385–412, 1997.
- 489 S. Michel, A. Gualandi, and J.-P. Avouac. Interseismic coupling and slow slip  
490 events on the Cascadia megathrust. *Pure and Applied Geophysics*, 176:3867–  
491 3891, 2019.
- 492 K. Obara. Nonvolcanic deep tremor associated with subduction in southwest  
493 Japan. *Science*, 296(5573):1679–1681, 2002.
- 494 R. Ohtani, J.J. McGuire, and P. Segall. Network strain filter: A new tool  
495 for monitoring and detecting transient deformation signals in GPS arrays.  
496 *Journal of Geophysical Research*, 115:B12418, 2010.
- 497 D.B. Percival and A.T. Walden. *Wavelet Methods for Time Series Analysis*.  
498 Cambridge Series in Statistical and Probabilistic Mathematics. Cambridge  
499 University Press, New York, NY, USA, 2000.
- 500 L.A. Preston, K.C. Creager, R.S. Crosson, T.M. Brocher, and A.M. Trehu.  
501 Intraslab earthquakes: Dehydration of the Cascadia slab. *Science*, 302:1197–  
502 1200, 2003.
- 503 G. Rogers and H. Dragert. Tremor and slip on the Cascadia subduction zone:  
504 The chatter of silent slip. *Science*, 300(5627):1942–1943, 2003.
- 505 D.R. Shelly, G.C. Beroza, and S. Ide. Non-volcanic tremor and low-frequency  
506 earthquake swarms. *Nature*, 446:305–307, 2007.
- 507 W. Szeliga, T.I. Melbourne, M.M. Miller, and V.M. Santillan. Southern Cas-  
508 cadia episodic slow earthquakes. *Geophysical Research Letters*, 31:L16602,  
509 2004.

- 510 W. Szeliga, T. Melbourne, M. Santillan, and M. Miller. GPS constraints on 34  
511 slow slip events within the Cascadia subduction zone, 1997-2005. *Journal of*  
512 *Geophysical Research*, 113:B04404, 2008.
- 513 E.K. Todd and S.Y. Schwartz. Tectonic tremor along the northern Hikurangi  
514 Margin, New Zealand, between 2010 and 2015. *Journal of Geophysical Re-*  
515 *search Solid Earth*, 121:8706–8719, 2016.
- 516 A.G. Wech. Interactive tremor monitoring. *Seismological Research Letters*, 81  
517 (4):664–669, 2010.
- 518 A.G. Wech. Extending Alaska’s plate boundary; tectonic tremor generated by  
519 Yakutat subduction. *Geology*, 44(7):587–590, 2016.
- 520 M. Wei, J.J. McGuire, and E. Richardson. A slow slip event in the south central  
521 Alaska Subduction Zone. *Geophysical Research Letters*, 39:L15309, 2012.
- 522 P. Wessel and W. H. F. Smith. Free software helps map and display data. *EOS*  
523 *Trans. AGU*, 72:441, 1991.

524      **Addresses**

525      Ariane Ducellier. University of Washington, Department of Earth and Space  
526      Sciences, Box 351310, 4000 15th Avenue NE Seattle, WA 98195-1310.

527      Kenneth C. Creager. University of Washington, Department of Earth and  
528      Space Sciences, Box 351310, 4000 15th Avenue NE Seattle, WA 98195-1310.

529      David A. Schmidt. University of Washington, Department of Earth and  
530      Space Sciences, Box 351310, 4000 15th Avenue NE Seattle, WA 98195-1310.

<sup>533</sup> **Tables**

Table 1: Big Episodic Tremor and Slip events. The duration and the number of tremor are from the tremor catalog of [reference?](#). The event number and the magnitude are from the slow slip catalog of Michel et al. [2019].

Time	Duration (days)	Number of tremor (hours)	Event number	Magnitude
2007.06	28	398	3	6.68
2008.36	25	402	10	6.56
2009.35	24	248	16	6.49
2010.63	29	518	24	6.54
2011.60	37	479	30	6.47
2012.72	37	620	34	6.54
2013.71	27	423	41	6.58
2014.65	15	190	48	6.03
2014.89	38	385	51	6.40
2016.11	43	421	54	6.79
2017.23	19	279	59	6.61
2018.49	22	381		
2019.23	34	195		
2019.88	16	205		
2020.79	26	193		
2020.86	12	162		
2021.09	14	230		

Table 2: Magnitude 5 events from Michel et al. [2019].

Time	Event number	Magnitude	Sub-event of bigger event
2007.06	1	5.64	Yes
2007.08	2	5.91	Yes
2008.38	11	5.50	Yes
2009.16	14	5.50	No
2009.36	17	5.32	Yes
2010.63	25	5.76	Yes
2011.66	31	5.61	Yes
2011.66	32	5.32	Yes
2012.69	35	5.56	Yes
2013.74	42	5.71	Yes
2014.69	49	5.31	Yes
2014.93	52	5.39	Yes
2016.03	57	5.80	Yes
2017.13	60	5.43	Yes
2017.22	61	5.37	Yes

534 **Figure captions**

- 535 • Figure1. Details and smooth of the wavelet decomposition of a synthetics  
536 signal with period 500 days and duration of the slow slip event equal to 2  
537 days (left), 5 days, 10 days, and 20 days (right).
- 538 • Figure2. Bottom: Data from GPS station PGC5 without missing values  
539 (black) and with missing values replaced by the sum of a straight line  
540 and a Gaussian noise component (red) for two locations of the missing  
541 values (left and right). Bottom to top: Corresponding ten details and  
542 smooths of the wavelet composition for the original data (black) and for  
543 the missing values replaced by the sum of a straight line and a Gaussian  
544 noise component (red).
- 545 • Figure3. Details and smooth of the wavelet decomposition of the longitudi-  
546 nal displacement recorded at GPS station PGC5.
- 547 • Figure 4. GPS stations used in this study (black triangles). The black  
548 line represents the 40 km depth contour of the plate boundary model by  
549 Preston et al. [2003]. The red triangles are the locations where we stack  
550 the GPS data. The small grey dots are all the tremor locations from the  
551 PNSN catalog.
- 552 • Figure 5. Details and smooth of the wavelet decomposition of the de-  
553 trended cumulative tremor count around the third northernmost location  
554 on Figure 3.
- 555 • Figure 6. Top: Stacked 8th level details of the wavelet decomposition of  
556 the displacement over all the GPS stations located in a 50 km radius of a  
557 given point, for the 16 locations indicated in Figure 3. Bottom: Opposite  
558 of the 8th level detail of the cumulative tremor count in a 50 km radius  
559 of a given point for the same 16 locations.
- 560 • Figure 7. Top: Stacked 7th level details of the wavelet decomposition of  
561 the displacement over all the GPS stations located in a 50 km radius of a  
562 given point, for the 16 locations indicated in Figure 3. Bottom: Opposite  
563 of the 7th level detail of the cumulative tremor count in a 50 km radius  
564 of a given point for the same 16 locations.
- 565 • Figure 8. Top: Stacked 6th level details of the wavelet decomposition of  
566 the displacement over all the GPS stations located in a 50 km radius of a  
567 given point, for the 16 locations indicated in Figure 3. Bottom: Opposite  
568 of the 6th level detail of the cumulative tremor count in a 50 km radius  
569 of a given point for the same 16 locations.
- 570 • Figure 9. Top: Sum of the stacked 6th, 7th and 8th level details of the  
571 wavelet decomposition of the displacement over all the GPS stations lo-  
572 cated in a 50 km radius of a given point, for the 16 locations indicated  
573 in Figure 3. Bottom: Opposite of the sum of the 6th, 7th and 8th level

574 details of the cumulative tremor count in a 50 km radius of a given point  
575 for the same 16 locations.

- 576
- 577 • Figure 10. ROC curve for the sum of the 6th, 7th, and 8th level details of  
578 the wavelet decomposition. The red cross marks the true positive rate and  
579 the false positive rate obtained with the thresholds used to make Figure  
9.
  - 580 • Figure 11. Top: Stacked 5th level details of the wavelet decomposition of  
581 the displacement over all the GPS stations located in a 50 km radius of a  
582 given point, for the 16 locations indicated in Figure 3.

583 **Figures**

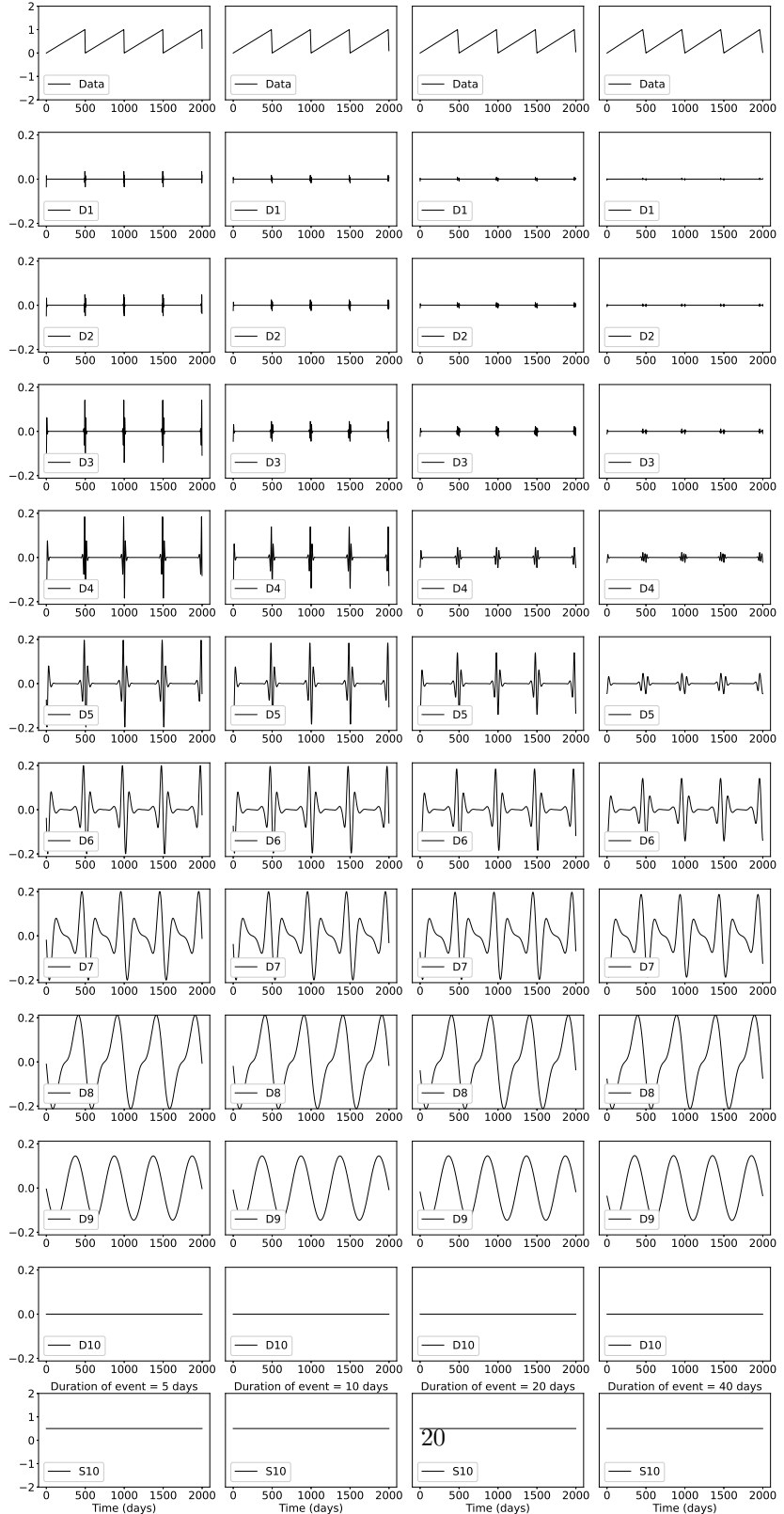


Figure 1: Details and smooth of the wavelet decomposition of a synthetics signal with period 500 days and duration of the slow slip event equal to 2 days (left), 5 days, 10 days, and 20 days (right).

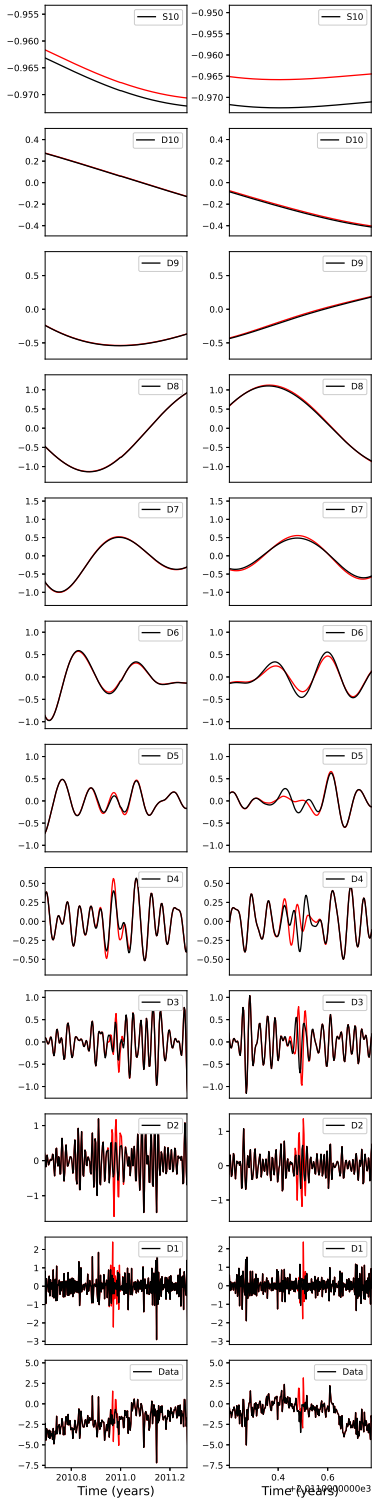


Figure 2: Bottom: Data from GPS station PGC5 without missing values (black) and with missing values replaced by the sum of a straight line and a Gaussian noise component (red) for two locations of the missing values (left and right). Bottom to top: Corresponding ten details and smooths of the wavelet composition for the original data (black) and for the missing values replaced by the sum of a straight line and a Gaussian noise component (red).

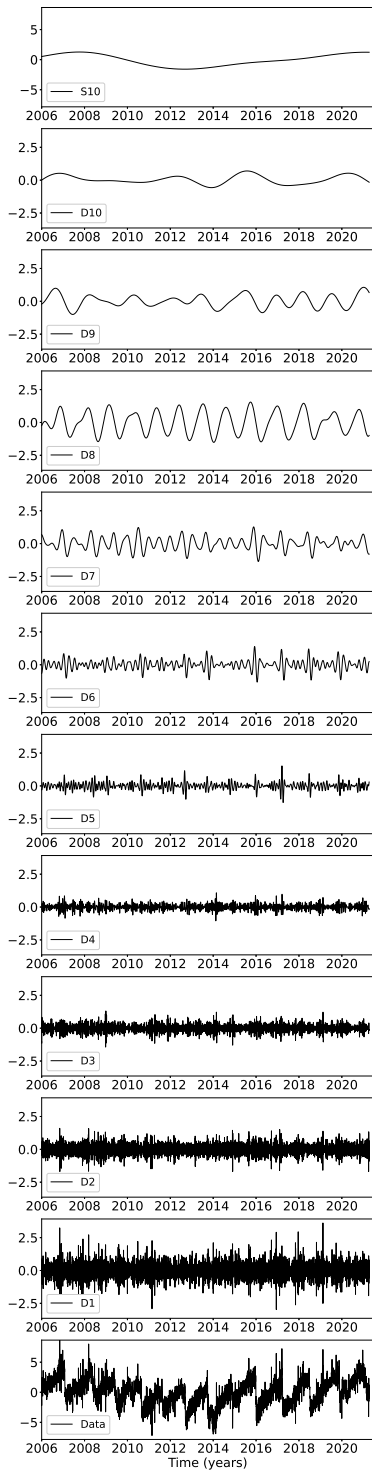


Figure 3: Details and smooth of the <sup>22</sup> wavelet decomposition of the longitudinal displacement recorded at GPS station PGC5.

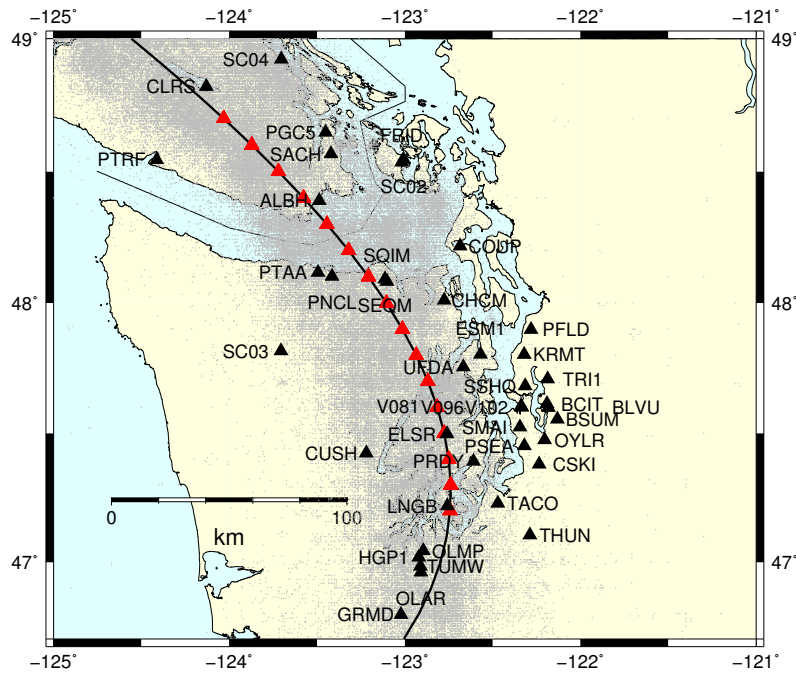


Figure 4: GPS stations used in this study (black triangles). The black line represents the 40 km depth contour of the plate boundary model by Preston et al. [2003]. The red triangles are the locations where we stack the GPS data. The small grey dots are all the tremor locations from the PNSN catalog.

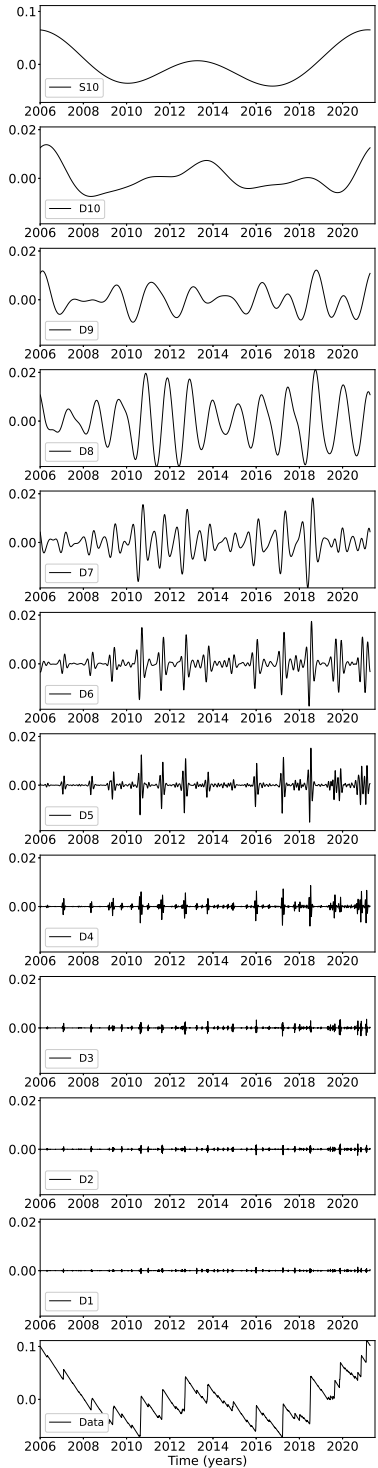


Figure 5: Details and smooth of the wavelet decomposition of the detrended cumulative tremor count around the third northernmost location on Figure 3.

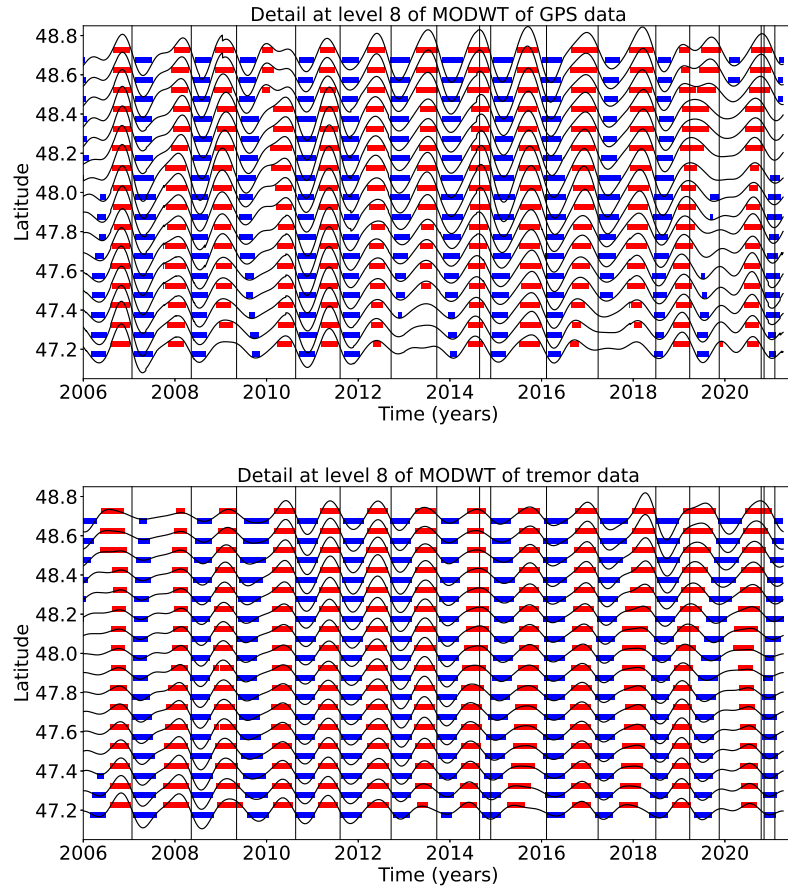


Figure 6: Top: Stacked 8th level details of the wavelet decomposition of the displacement over all the GPS stations located in a 50 km radius of a given point, for the 16 locations indicated in Figure 3. Bottom: Opposite of the 8th level detail of the cumulative tremor count in a 50 km radius of a given point for the same 16 locations.

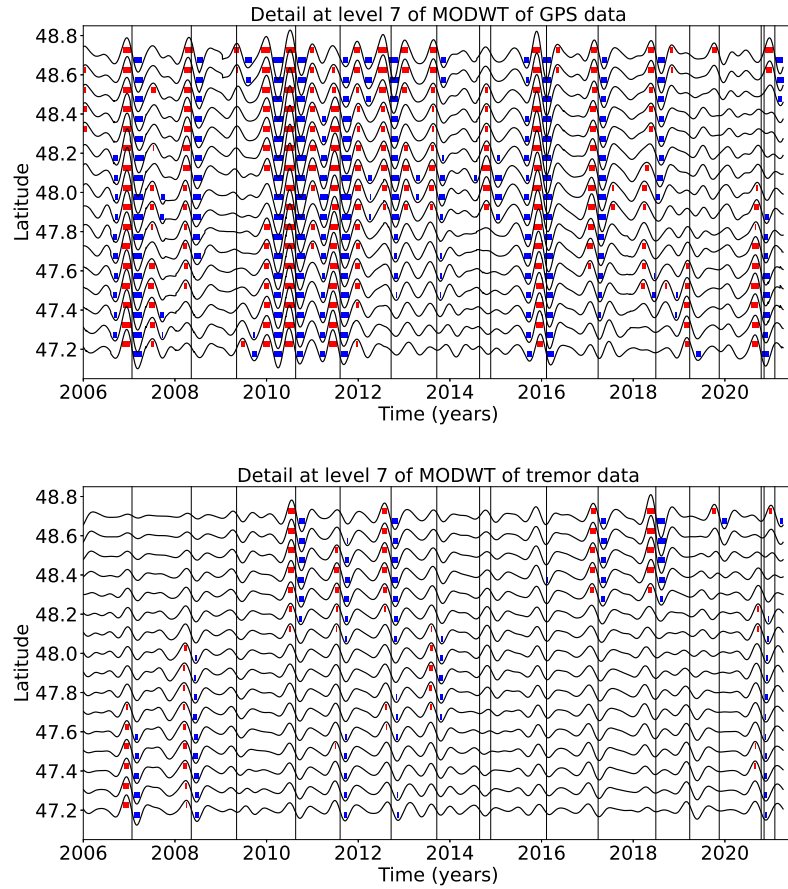


Figure 7: Top: Stacked 7th level details of the wavelet decomposition of the displacement over all the GPS stations located in a 50 km radius of a given point, for the 16 locations indicated in Figure 3. Bottom: Opposite of the 7th level detail of the cumulative tremor count in a 50 km radius of a given point for the same 16 locations.

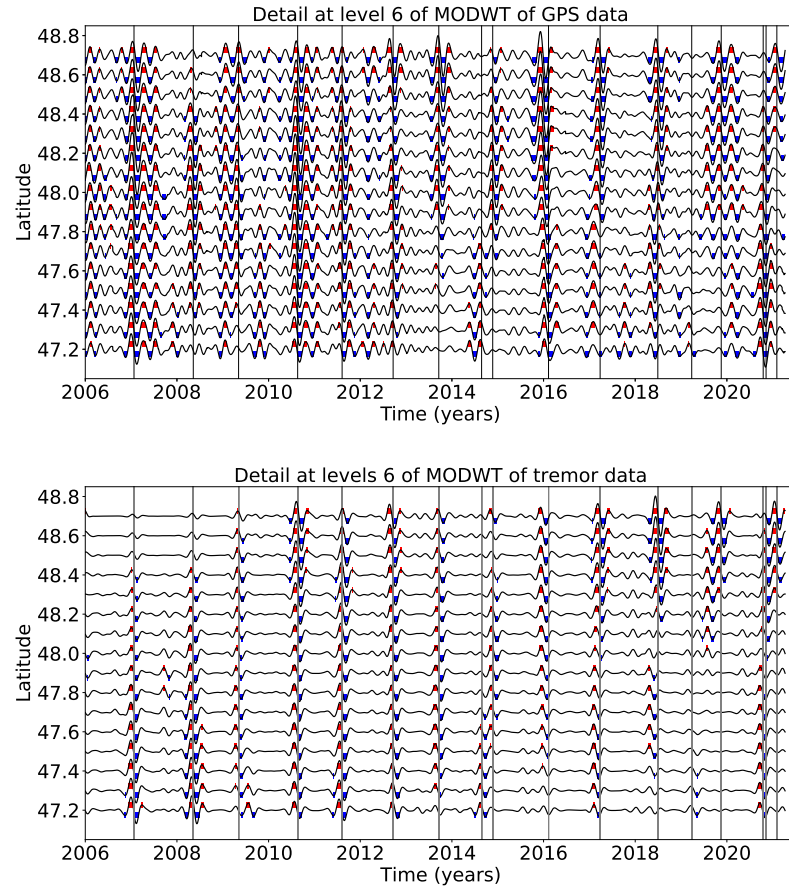


Figure 8: Top: Stacked 6th level details of the wavelet decomposition of the displacement over all the GPS stations located in a 50 km radius of a given point, for the 16 locations indicated in Figure 3. Bottom: Opposite of the 6th level detail of the cumulative tremor count in a 50 km radius of a given point for the same 16 locations.

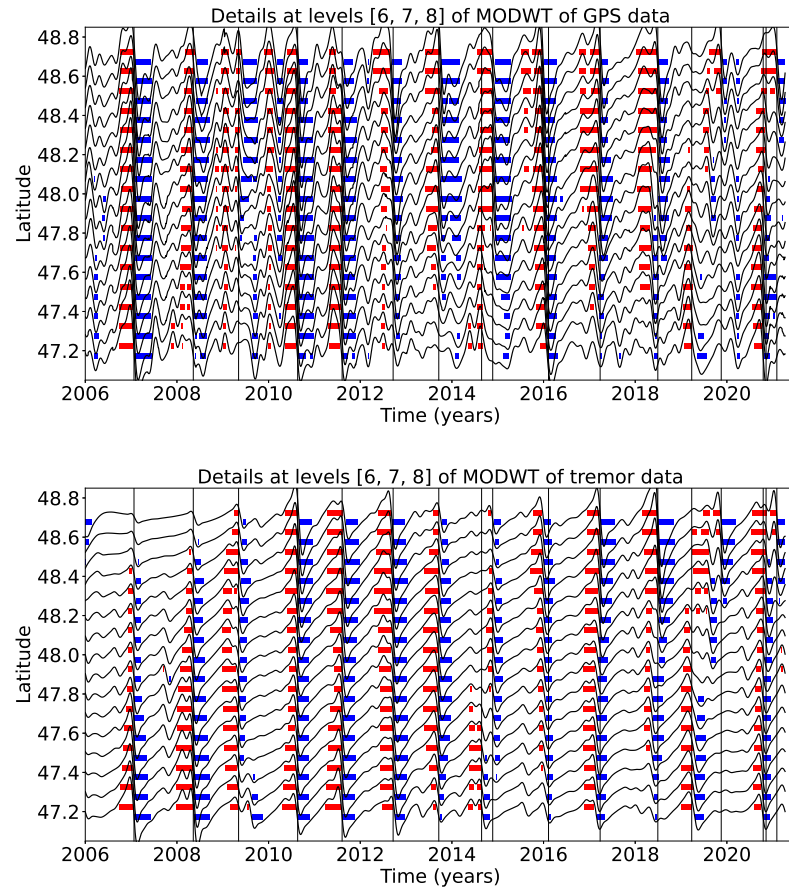


Figure 9: Top: Sum of the stacked 6th, 7th and 8th level details of the wavelet decomposition of the displacement over all the GPS stations located in a 50 km radius of a given point, for the 16 locations indicated in Figure 3. Bottom: Opposite of the sum of the 6th, 7th and 8th level details of the cumulative tremor count in a 50 km radius of a given point for the same 16 locations.

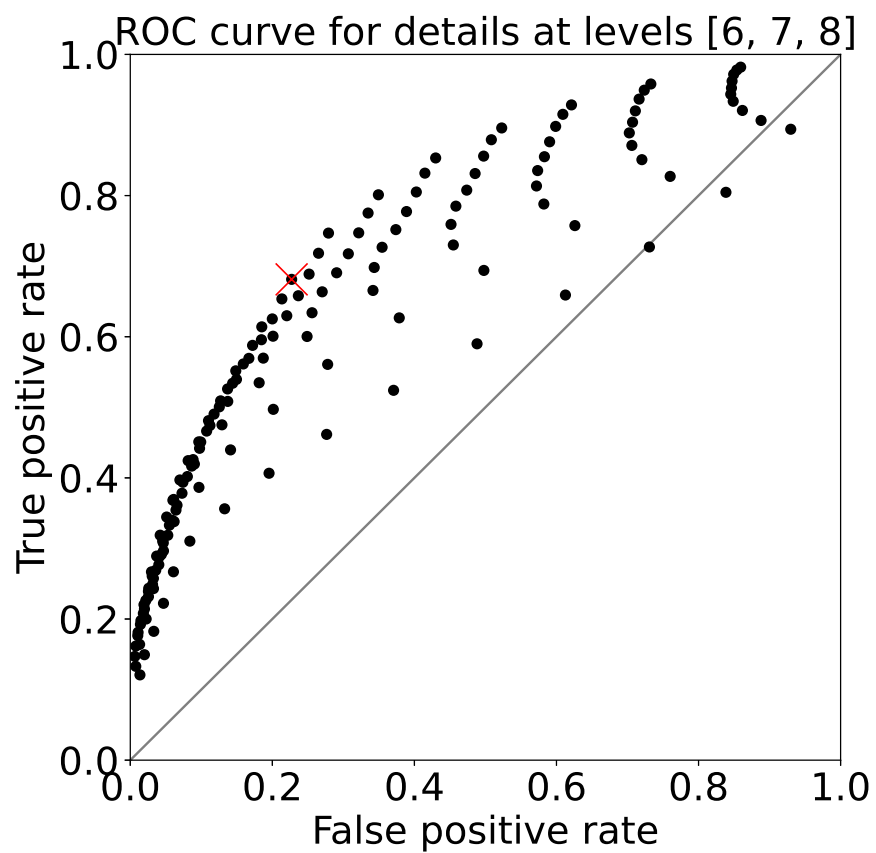


Figure 10: ROC curve for the sum of the 6th, 7th, and 8th level details of the wavelet decomposition. The red cross marks the true positive rate and the false positive rate obtained with the thresholds used to make Figure 9.

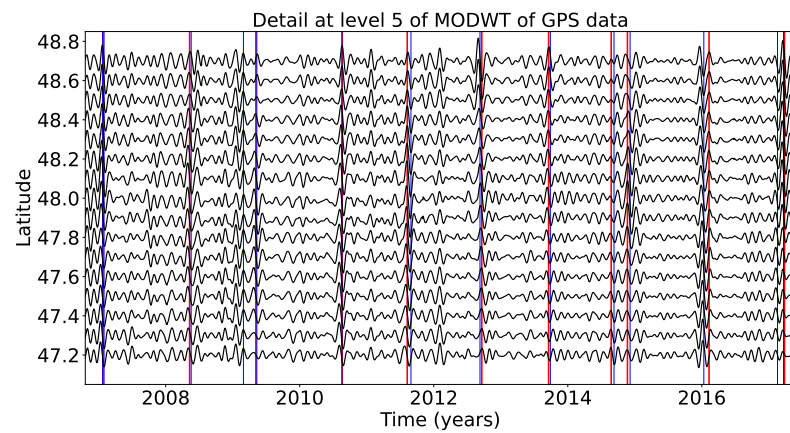


Figure 11: Top: Stacked 5th level details of the wavelet decomposition of the displacement over all the GPS stations located in a 50 km radius of a given point, for the 16 locations indicated in Figure 3.